Simultaneous free-surface deformation and near-surface velocity measurements

D. Dabiri, M. Gharib

Abstract A newly developed non-intrusive approach has been devised for studying near-surface flows where it is important to be able to construct correlations between small-sloped free-surface deformations and near-surface velocities. This method combines digital particle image velocimetry (DPIV) and the reflective mode of the free-surface gradient detector (FSGD) technique into a single measurement system, providing us with an approach to be able to characterize correlations between elevation and kinematic properties, such as velocity and vorticity, which is essential in understanding near surface turbulence. Furthermore, as the free-surface elevation is directly proportional to the pressure for low Froude number flows, this method will allow for the measurement of pressure near the free surface. This will also be useful in calculating the pressure-velocity term in the turbulent kinetic energy equation for near-surface flows. The approach is explained and demonstrated by measuring these correlations for a vertical shear layer intersecting a free surface.

1
Introduction

Free-surface flow phenomena are a subject of great interest as their effects can be seen both in nature and in matters of practical importance. Wave breaking, both spilling and plunging, is responsible for large air, and therefore oxygen, entrainment into the oceans, and is therefore a major contributor to the existence of life within the oceans. From a more practical view, ship wakes have been known to persist for over several hundred kilometers, thus making them detectable to different remote sensing techniques. In order to understand these phenomena, it is important to understand not only the fluid mechanics beneath the free surface, but also the free-surface deformation, and their interaction with each other. The interaction of the free

D. Dabiri, M. Gharib
Graduate Aeronautics Laboratories
California Institute of Technology, Pasadena, CA 91125, USA
e-mail: dabiri@caltech.edu

Correspondence to: D. Dabiri

surface with the near-surface turbulence is by no means simple. The near-surface turbulence causes deformations of the free surface, thereby storing energy in this deformation. When the deformation relaxes, energy is then released back into the fluid, thereby affecting the near-surface turbulence. Should the deformations be large, it is possible for the deformations to release their energy in the form of radiating waves that travel away, thereby affecting the near-surface flow elsewhere. To understand these phenomena, it is important to be able measure both the near-surface velocity, and the free-surface deformation simultaneously, at least within a two-dimensional domain, in order to obtain insights into the physics of such interactions.

While velocity measurements have enjoyed dramatic progress through the development of DPIV techniques, it is only recently that free-surface measurements have been developed to the degree that would allow for both spatial and temporal measurements. Cox (1958) first developed a single point, single slope component detector, capable of measuring water slopes through time. More recently, Zhang and Cox (1994) and Zhang (1995), using a discretized color palette, developed a FSGD based on a refractive color encoding scheme, capable of measuring two slope components for a given area at a single point in time for short wind wave studies. For more accurate results, Jähne (1997) and Balschbach et al. (1998) incorporated a continuous color palette with the refractive FSGD technique. Such gradient and elevation schemes are a subset of the more general shape-from-shading techniques as explained by Klette et al. (1998).

Initially, these methods, which relied on image acquisition, were applied to single photographic images. However, with the advent of technology, it became possible to apply these methods to data acquired through video technology, and thereby attain time-evolving results. For example, a real-time acquisition version of the refractive color-encoding method using a discretized color palette was developed for the study of time-evolving free-surface deformations (Zhang et al. 1996; Dabiri et al. 1997). In a clever approach, Hering et al. (1996) and Wierzimok et al. (1996) obtained both free-surface elevation results and particle paths from sparsely seeded flows, using a combined digital particle tracking velocimetry method (DPTV) and a refractive color-encoding FSGD technique. Since waves were studied, the refractive color-encoding scheme was used, as it was necessary to resolve large slopes.

Interestingly, the work of Dommermuth et al. (1994) provides a method whereby the near-surface pressure field

can be obtained through the free-surface deformation field. In their study, it is shown that by looking at low Froude number flows, it is possible to express the equations of motion as

$$\frac{\partial U_i^{\mathrm{r}}}{\partial \tilde{t}} + U_j^{\mathrm{r}}\frac{\partial U_i^{\mathrm{r}}}{\partial x_k} = -\frac{\partial P^{\mathrm{r}}}{\partial \tilde{x}_i} + \frac{1}{Re}\frac{\partial^2 U_i^{\mathrm{r}}}{\partial x_j^2} + \alpha f(U_i^{\mathrm{r}})\frac{\partial U_i^{\mathrm{r}}}{\partial \tilde{x}_i} = 0 \;\; ;$$

$$\frac{\partial^2 P^{\mathrm{r}}}{\partial x_j^2} = -\frac{\partial U_j^{\mathrm{r}}}{\partial \tilde{x}_i}\frac{\partial U_i^{\mathrm{r}}}{\partial \tilde{x}_j} \;\; \text{for} \;\; \tilde{z} \le 0 \;\; ;$$

$$W^{\mathrm{r}} = 0 \quad \text{and} \quad \frac{1}{Fr^2}\eta^{\mathrm{r}} = -P_{\mathrm{a}} + P^{\mathrm{r}} \quad \text{for} \quad \tilde{z} = 0$$

where the superscript r refers to components that contribute to the free surface roughness, η is the free-surface elevation, P is the pressure normalized by the density, U is the velocity, the subscript a refers to atmospheric conditions, α is a source coefficient, and W is the vertical velocity component and f is a linear operator. Most interesting is the last of these equations that shows that with the neglect of the atmospheric pressure, the surface elevation is hydrostatically balanced by the vortically-induced pressure. This insight provides us with a way to measure near-surface pressures through the measure of free-surface elevations.

To better understand free-surface flows, as a first step, we propose to examine the interaction of the free surface with the near-surface turbulence without the added complexity of wave radiation due to steep slopes. However, for small free-surface deformations, the refractive FSGD will not provide enough resolution to properly map out the deformation field. It is therefore the intent of this paper to present a combined technique that incorporates a real-time digital free-surface reflective gradient detector (FSGD) system with DPIV, to provide simultaneous, time-evolving flow and surface deformation fields for free-surface flows with small deformation slopes. As will be shown below, this is important in terms of identifying correlations between surface elevation and various kinematic properties, as well as being able to calculate the near surface pressure spectra.

2
Free surface gradient detector

2.1
Operating principle
The operating principle behind the FSGD is to color code the different slopes of the free surface with different colors in order to establish a one-to-one correspondence between color and slope (Dabiri et al. 1997; Zhang et al. 1996; Zhang and Cox 1994). There are basically two modes that can be employed. The refractive mode is used for cases where the slope variations are large, while the reflective mode is used for cases where slope variations are small. For the present setup, the reflective mode is used since the range of free surface slopes was small.

The principle of the reflective mode is shown in Fig. 1. A color palette, when placed in front of a diffused white light source, will illuminate each of the colors in all di-

rections. When a lens is placed at a distance of one focal length away from the color palette, all of the rays of each color will become parallel; yet will be oriented in different directions with respect to other colored light rays. This setup will then create a system of parallel color beams, which is used to illuminate the free surface. Figure 2 shows how the different free-surface slopes are color-coded. When the free surface is illuminated with the parallel color beams, there is only one free surface slope that will reflect a particular color towards an observer located far away. In this way, a one-to-one correspondence is achieved between color and free-surface slopes.

2.2
Color palette
For a reflective system, the angle of the reflected beams from the free surface is equal to the incident angle onto the free surface. Therefore, as shown in Fig. 3, the largest angle that can be measured, $\alpha_{\max}$, is a function of the diameter of the lens, D, its focal length, f, and the diameter of the color palette, D_{s}:

$$\alpha_{\max} = \tan^{-1}\left(\frac{D_{\mathrm{s}}}{2f}\right) \le \tan^{-1}\left(\frac{D}{2f}\right) = \tan^{-1}\left(\frac{1}{2F\#}\right) \;\; . \tag{1}$$

When the size of the palette is equal to the size of the lens, the maximum measurable angle can be determined by the $F\#$ of the lens. The maximum measurable area denoted by $L_{\max}$ depends on the size of the lens, D, the angle between the optical axis and the free surface normal, β_0, the normal distance from the center of the lens to the free surface, H, and the largest possible angle between the light rays and the free surface normal, $\beta_{\max}$ (see Fig. 3), and is given by the relation:

$$L_{\max} = D\cos\beta_0 - \left(H - \frac{D}{2}\sin\beta_0\right)\tan\beta_{\max}$$
$$- \left(H + \frac{D}{2}\sin\beta_0\right)\tan(\beta_{\max} - 2\beta_0) \;\; . \tag{2}$$

A sample color palette used is shown in Fig. 4. Given this color palette, the dimension of each of the color elements can be denoted by δe. Therefore, the smallest angle change that can be measured is

$$\delta\alpha \le \tan^{-1}(\delta e/f) \;\; , \tag{3}$$

and is defined as the slope sensitivity. The viewing angle of the camera is

$$\psi = \tan^{-1}(D_{\mathrm{c}}/L) \;\; , \tag{4}$$

where D_{c} is the diameter of the camera lens, and L is the total length from the free surface to the camera. To prevent any super-positioning of the adjacent colors, the camera-viewing angle must be less than the slope sensitivity:

$$\frac{D_{\mathrm{c}}}{L} \le \frac{\delta e}{f} \;\; . \tag{5}$$

The color palette shown in Fig. 4 had two problems. First, the discrete nature of the color palette limited the number
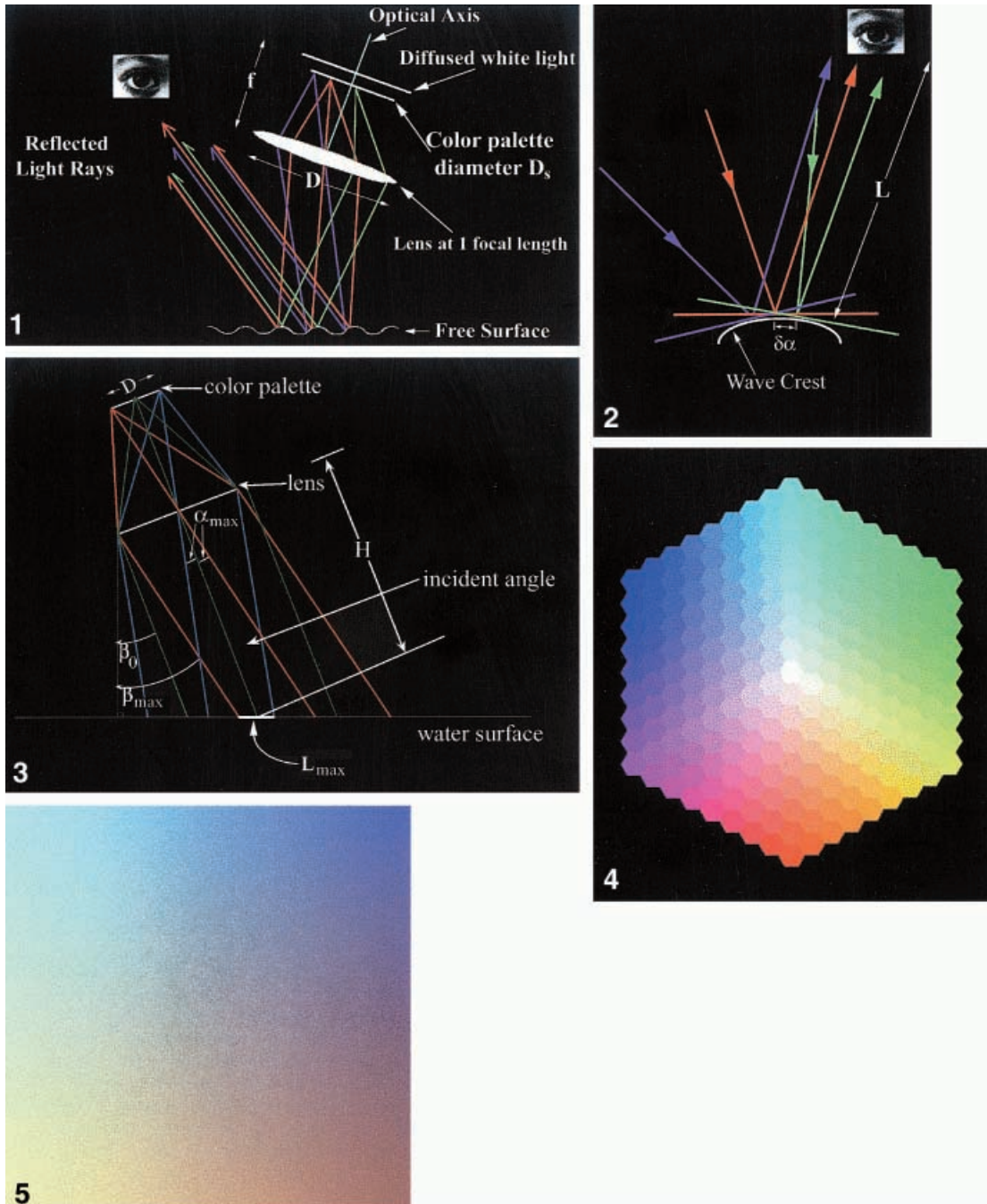
Fig. 1. Reflective mode setup of the free-surface gradient detector
Fig. 2. Reflective mode close-up showing the color-coding mechanism
Fig. 3. Optical setup and ray tracing showing the measurable area of the free surface
Fig. 4. Discrete color palette
Fig. 5. Continuously varying color map

of colors (and hence slopes) that could be measured. Second, the intensity variations resulted in poor measurements for low intensity colors. Therefore, a new continuously varying color map shown in Fig. 5 as proposed by Jähne (1997) and Balschbach et al. (1998) is used. The colors are designed so that green varies linearly in the x-direction, and red and blue vary linearly in the y-direction. Each of these colors is then normalized and recombined so that

$$3G/(R + G + B) \ , \tag{6}$$

varies linearly in the x-direction, and

$$3(R - B)/(R + G + B) \ , \tag{7}$$

varies linearly in the y-direction. Since this color palette is continuous and normalized by the intensity, it has the advantage of increasing the slope sensitivity as well as compensating for spatial intensity variations.

2.3
Calibration

In order to convert from the color images to the free-surface slopes, it is necessary to create a lookup table by performing a calibration. It is important that the calibration be done in the exact same setup as the experiment, as the data acquired is highly dependent on the setup of the FSGD. The calibration is performed by first placing a spherical mirror of known curvature within the desired measurable area. The FSGD illuminates the spherical mirror, and the rays collected by the color camera from the spherical mirror are saved as the color calibration image. Since the slopes of the spherical mirror are known, a lookup table can be easily constructed using the colors and their corresponding slopes.

2.4
Free surface elevation extraction

The acquired images are slightly noisy due to the camera's electronics and the low lighting. Therefore, the first step is to pre-process the images by applying a median filter. Once the digitization noise is removed, the color images are converted to free surface slopes using a lookup table, described in the previous section. The free surface elevation is then derived by integrating the slopes in the Fourier domain. Any function, f, can be represented by its Fourier transform

$$f(x, y) \iff F(k_x, k_y) \ . \tag{8}$$

The derivatives of this function can be represented as a function of the Fourier transform of f,

$$f_y(x, y) \iff ik_y F(k_x, k_y) = F_y(k_x, k_y) \ , \tag{9}$$

$$f_x(x, y) \iff ik_x F(k_x, k_y) = F_x(k_x, k_y) \ . \tag{10}$$

By rearranging and combining Eqs. (9) and (10), the free surface elevation can be calculated as:

$$f(x, y) + C \iff F(k_x, k_y)$$
$$= \frac{F_x(k_x, k_y) \cdot (-ik_x) + F_y(k_x, k_y) \cdot (-ik_y)}{k^2} \ , \tag{11}$$

where C is the constant of integration, and must be determined a priori. This approach has been previously recommended and used by Zhang and Cox (1994), Zhang (1995, 1996), Zhang et al. (1996), Dabiri et al. (1997) and Balschbach et al. (1998).

3
Digital particle image velocimetry (DPIV)

The DPIV processing technique used is a cross-correlation technique described by Willert and Gharib (1991), incorporating the window-shifting technique developed by Westerweel et al. (1997). As DPIV has been well documented, full details of it shall not be discussed in this paper, and the reader is referred to Gharib and Dabiri (1999) and its references for a full explanation of cross-correlation DPIV. Below, we give a brief outline of the DPIV technique used, and its associated uncertainties.

The DPIV technique involves seeding the flow with optically reflective particles. Pulsed lasers (typically Nd:YAG lasers) are used to create a laser sheet to illuminate the cross-section of interest. A digital video camera captures sequential, singly-exposed images of the illuminated particle fields. For analysis, an interrogation window subsamples identical portions of sequential image pairs. By calculation of a cross-correlation for the local interrogation window, a local velocity vector is obtained. Upon systematic scanning of the images with the interrogation window, a velocity vector field is thus obtained.

Since the particles move within the interrogation window, the number of particles common to both sequential images is less than the total particles within each of the windows, hence resulting in an uncertainty of $\sim$3 and $\sim$6% in the velocity and vorticity measurements, respectively. By locally moving the interrogation window in the second of the sequential image pairs, using the DPIV results from the stationary interrogation window as a guide, it is possible to increase the number of the particles common to both sequential images. This procedure boosts the signal-to-noise ratio so that the velocity and vorticity measurement uncertainties are within 1% and 2%, respectively (Dabiri et al. 1995).

4
Experimental setup

The experiment is done within a free-surface shear layer facility in order to measure both the free-surface deformation due to the interaction of the shear layer with the free surface, and the flow field directly below the free surface. The test section of the tunnel is 2-m long, 1-m wide, and 0.75-m high (see Fig. 6). At rest, the fluid level is 0.56-m high. Neutrally buoyant, silver-coated glass sphere particles with an average diameter of $14 \pm 5 \, \mu m$ are used to seed the flow. For the DPIV measurements, dual Nd:YAG lasers and appropriate optics are used to generate a planar light sheet parallel to the free surface. The light sheet is 1-mm thick and is located just below the free surface to map out the near surface flow field. The time difference between the exposures is 2 ms. The DPIV images are 1008×1018 pixels, and are processed using a 32×32 pixels window size with a 50% window overlap. All images acquired are recorded at 30 frames/s onto a real-time digital recorder.

As the setup of the technique is sensitive to the geometry of the set-up for the FSGD technique, both the calibration and the experiment are done with the same set-up and within the same experimental facility. In order to be able to measure free-surface deformations of large areas, it is necessary to use a large lens. Unfortunately, large lenses with low F#'s and good performances are quite costly. So it is most effective to replace the lens with a mirror, which has the added advantage of eliminating inaccuracies due to chromatic aberrations. The free-surface gradient detector setup is shown in Fig. 7. It is designed to allow for ease of adjustment of the distance between the mirror, color palette, and the light source, as well as the angle of this setup with respect to the free surface. The color palette used is shown in Fig. 5, and is $10.16 \times 10.16 \, cm^2$. The mirror used is a 20.32-cm diameter front surface coated spherical mirror, with a 60.96-cm focal length. A linear xenon strobe light is used for illumination, since xenon provides a relatively uniform spectral response across the visible spec-
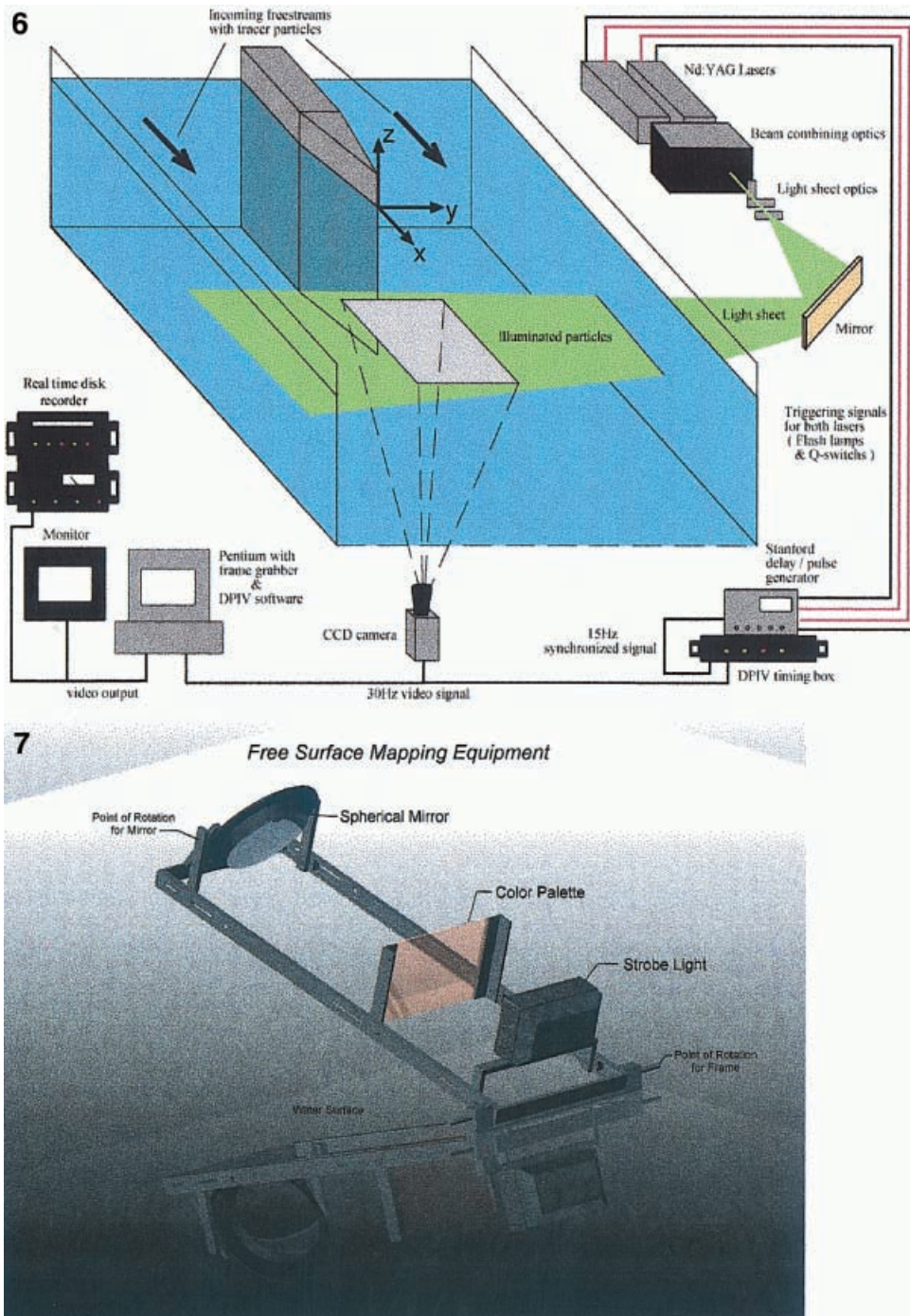
Fig. 6. Free shear tunnel facility with DPIV experimental setup
Fig. 7. Free-surface gradient detector setup

trum. The elevation range measured is ± 1.2 mm with a maximum measurement uncertainty of 6%.

To ensure simultaneous acquisition of both free surface deformation and the near surface velocity field, it is necessary to synchronize the DPIV camera with the FSGD camera. This is achieved by using the horizontal and vertical drives of the DPIV camera to drive the horizontal and vertical drives of the FSGD camera, respectively. Figure 8 shows the pulse sequence of both the DPIV and FSGD cameras and their proper placements in relation to each other to ensure simultaneous data acquisition. Also, to ensure proper alignment of the two acquisition cameras, first, the superimposed, live images from both cameras are used to coarsely align the imaged areas. Then, four points located at the corners of a "+" are simultaneously acquired by both systems. The centers of these points are then determined to within 1/10th of a pixel using a one-dimensional Gaussian curve fit about the peak of each of these points in both the x- and y-directions. Lastly, the sizes and locations of the "+"'s mapped out by the four points in each of the alignment images is used to determine and correct for the magnification, translation, and rotational differences between the two data sets.

Figure 9 shows the format in which the data was taken and will be presented. The high-speed side is on the left and is 22.5 cm/s while the low-speed side is on the
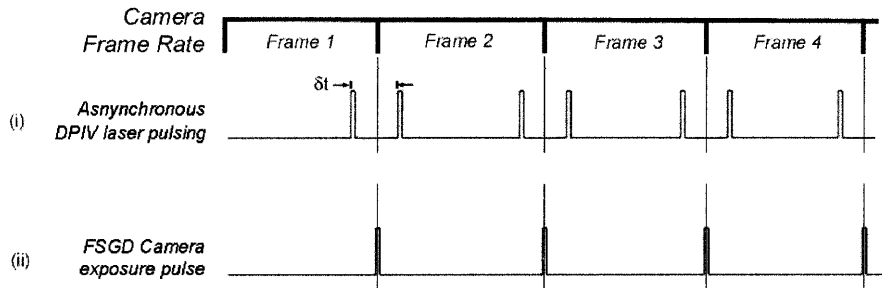
Camera Frame Rate

| Frame 1 | Frame 2 | Frame 3 | Frame 4 |

(i) Asynchronous DPIV laser pulsing

δt →|

(ii) FSGD Camera exposure pulse

Fig. 8. Exposure sequence and synchronization for the DPIV and FSGD cameras
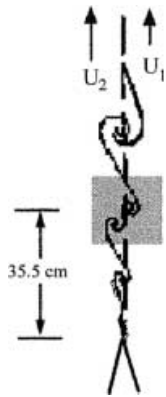
386

U_2 U_1

35.5 cm

Fig. 9. Format in which the data is taken. High-speed side is on the left, while the low-speed side is on the right

right and is 10.6 cm/s. The center of the imaged are is 35.5 cm downstream from the splitter plate, and the flow as shown is from bottom to top. The Reynolds number based on the average velocity of the two streams and the vorticity thickness of the shear layer at the surface at mid-image is 7425, and the Froude number based on the depth of the water channel is 0.07. At these velocities, the deformations are not severe, as there are no wave breaking, or capillary waves generated, thereby making the use of the reflective mode optimal.

5
Error analysis
As the sources of error for DPIV are well documented, the reader is again referred to Gharib and Dabiri (2000) and its references for more information. For the FSGD set-up, the sources of error that contribute to the uncertainty of the measurements can be broken down into two parts, optical errors and processing errors.

The optical errors can be sub-divided into four parts, chromatic aberrations, spherical aberrations, coma, and astigmatism. Chromatic aberrations arise when there are multiple frequencies that refract through a lens. Since the focal capabilities of the lens are a function of the index of refraction, which in turn is a function of color, or frequency, various colors will focus at various points along the optical axis. Spherical aberrations correspond to a dependence of focal length or aperture for nonparaxial rays. This implies that, for an incoming bundle of monochromatic parallel rays aligned with the optical axis, the focal points on the optical axis will be a function of the ray height from the optical axis at the lens. Comatic aberra-

tions arise when a point off-axis on the object plane focuses to various points on a vertical plane in the image plane, due to the fact that the focus is also a function of the ray height from the optical axis at the lens. Lastly, astigmatism refers to aberrations arising when a cone of rays strikes a lens asymmetrically, thereby resulting in two distinct focal lengths. Since the colored beams are reflected by a mirror rather than refracted by a lens, chromatic errors are entirely avoided. However, since the present setup is an off-axis set-up with a spherical mirror, all the other aberrations will contribute to uncertainties within the present system. It should be pointed out that since a continuous color palette is used, the adverse effects of these aberrations can be reduced (Zhang and Cox 1994) by taking advantage of the fact that due to the optical aberrations, colors from the color palette, when imaged, will be locally averaged onto each pixel. Therefore, since the color palette is continuous and linear, the resulting averaged color will be close to a color unaffected by aberrations, thereby minimizing the effects of the aberrations just described.

The processing errors have been discussed in depth by Zhang (1996). Most importantly, it is shown that the data, after conversion to the Fourier domain, must be artificially extended to a larger area so that the periodic boundary values change without discontinuities by reflecting the data set across each boundary. Therefore, if the slopes in the x- and y-directions are defined as

$$f_x(x,y) = X(x,y) \quad \text{and} \quad f_y(x,y) = Y(x,y) , \qquad (12)$$

for a domain

$$\lfloor (0, L_x), (0, L_y) \rfloor , \qquad (13)$$

then the data sets are extended such that

$$f_x(x,y) = X(-x,y) \quad \text{and} \quad f_y(x,y) = Y(-x,y)$$
$$\text{for } \lfloor (-L_x, 0), (0, L_y) \rfloor , \qquad (14)$$

$$f_x(x,y) = X(x,-y) \quad \text{and} \quad f_y(x,y) = Y(x,-y)$$
$$\text{for } \lfloor (0, L_x), (-L_y, 0) \rfloor , \qquad (15)$$

$$f_x(x,y) = X(-x,-y) \quad \text{and} \quad f_y(x,y) = Y(-x,-y)$$
$$\text{for } \lfloor (-L_x, 0), (-L_y, 0) \rfloor . \qquad (16)$$

Zhang showed that by implementing this scheme, the processing uncertainties can be reduced by two orders of magnitude. It should be pointed out, however, that implementing this scheme increases the data set by a factor of four, thereby increasing the computational time and space dramatically.

At present, no effort has been made to identify the individual contributions of each of these sources of error to the measurement uncertainties. Rather, an overall error was determined by placing a spherical mirror of known curvature at various parts of the measurable area. Images were then obtained, from which the elevations were calculated, and compared with their true elevations. These differences were then statistically analyzed, showing a maximum measurement uncertainty of 6%. As the velocity and vorticity uncertainties are 1 and 2%, respectively, the uncertainties of the elevation/velocity and elevation/vorticity correlations are 6.1 and 6.3%, respectively.

6
Data analysis and discussion
To demonstrate the capabilities of this technique, preliminary results showing the correlations of the free-surface elevation with the near-surface flow field are presented. More detailed discussions of these results are given in Dabiri (2000). Figures 10 and 11 show a processed FSGD elevation field, and its near-surface vorticity field at an instance in time. It can be seen that the regions of high vorticity correspond to regions of free-surface deformation. Most noticeable are the two regions of high vorticity, labeled *a* and *b* in Fig. 11, which are vortex tubes connected to the free surface. These vortex tube connections are responsible for a free-surface deformation "dimples", labeled *a* and *b*, as shown in Fig. 10.

Even though the instantaneous correlation shown above is striking, it is more appropriate to perform this correlation through time. To show these results, the last series of plots are rearranged so that the high speed side is on the right, while the low speed side is on the left. Furthermore, the dividing stream line is set as the origin of the spanwise
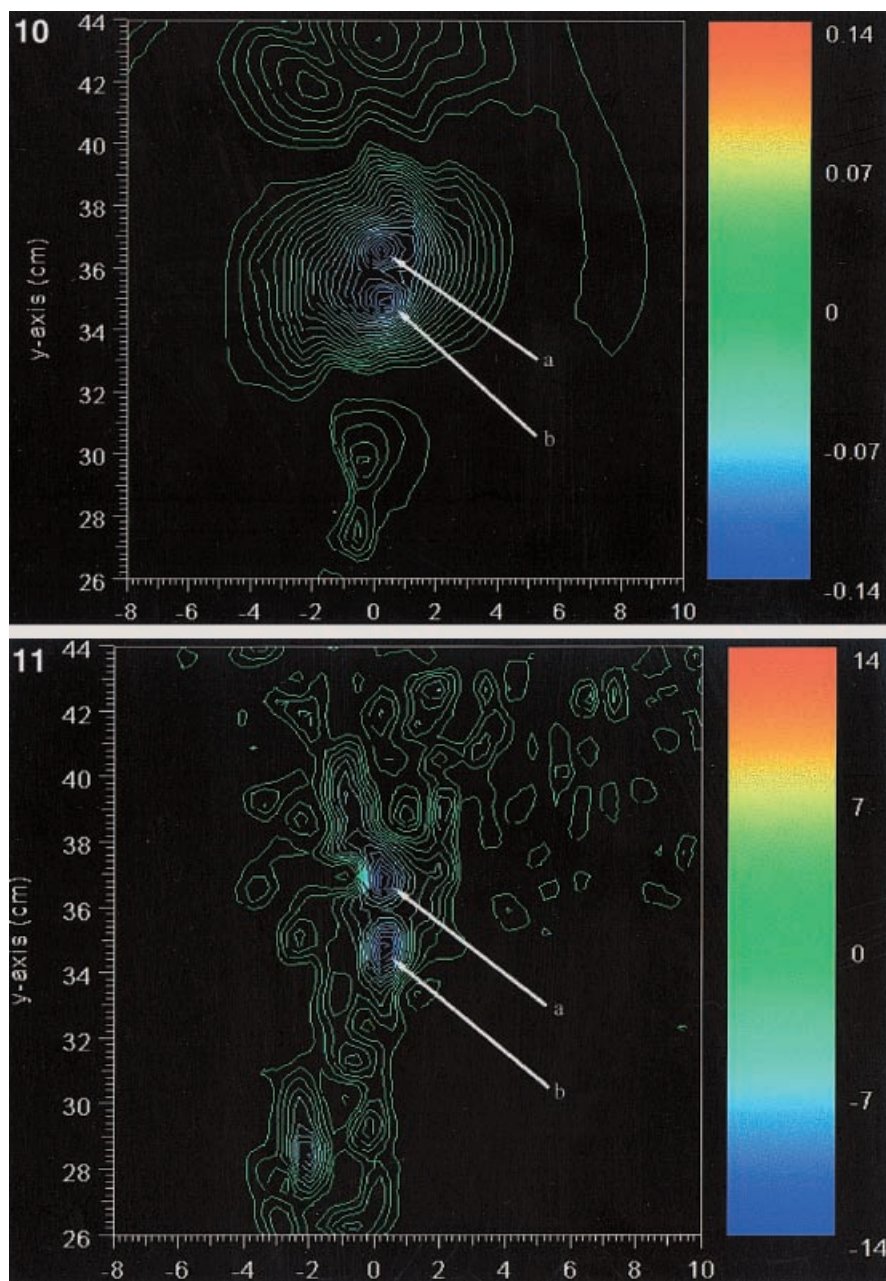
Fig. 10. An instantaneous free-surface elevation plot. Contours are 0.014 cm per level. Axes are in cm

Fig. 11. Near-surface instantaneous vorticity plot. Axes are in cm

direction (shown on the *x*-axis of the plots). The spanwise direction is then normalized by the local vorticity thickness. Six downstream spanwise profiles are plotted within the range $x \in [26, 46]$ cm. Figure 12 shows the normalized streamwise velocity profiles, demonstrating that the flow has achieved a self-preserving state in the mean. Figures 13 and 14 show the normalized correlation and the correlation coefficient between the free-surface deformation fluctuations and near-surface streamwise velocity fluctuations, respectively. While Fig. 13 shows that there are maximum correlations at $\lambda \approx \pm 0.3$, as shown in Fig. 14, these correlations are not very strong since their correlation coefficients are $\sim \pm 0.2$. Figures 15 and 16 show the normalized correlation and the correlation coefficient between the free-surface deformation fluctuations and near-surface spanwise velocity fluctuations, respectively. Figure 15 shows that correlations grow on either side of the dividing streamline. However, the correlation coefficients reach a maximum value of ~ 0.25, indicating that these correlations are not strong. Lastly, Fig. 17 and 18 show the normalized correlation and the correlation coefficient between the free-surface deformation fluctuations and the near-surface vertical vorticity component
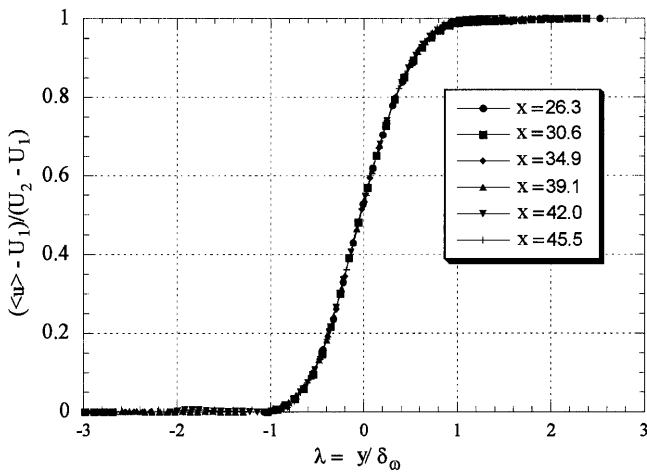
fluctuations, respectively. Figure 17 shows that correlations grow with downstream distance within $\lambda = [-1, 0.5]$, and that the spanwise correlation peaks are slightly shifted

Fig. 14. Mean streamwise velocity/elevation correlation coefficient profiles at various downstream locations

Fig. 15. Mean normalized spanwise velocity/elevation correlation profiles at various downstream locations

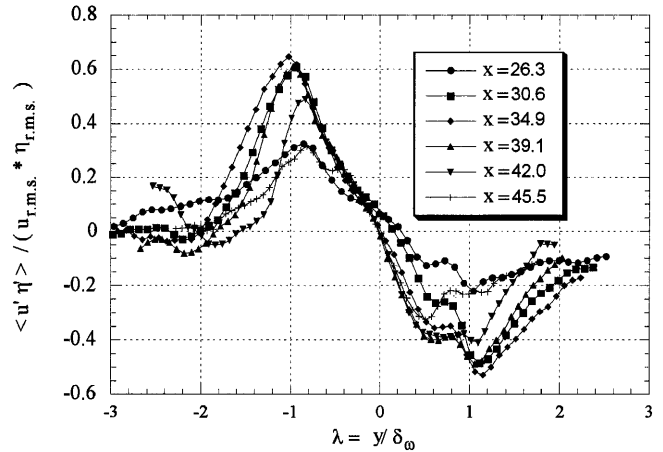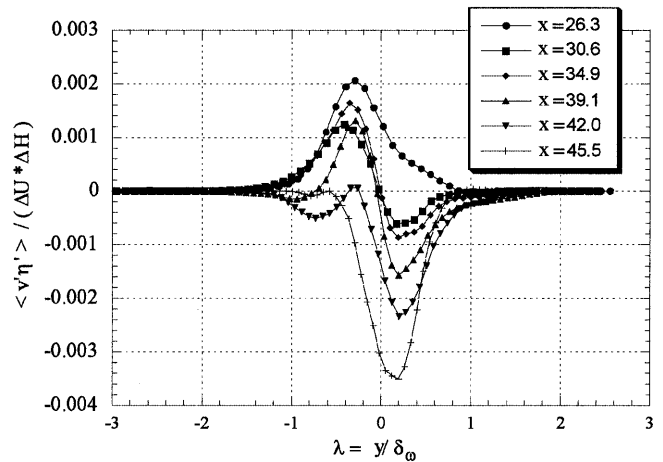**Fig. 12.** Mean normalized vertical vorticity profiles at various downstream locations

Fig. 13. Mean normalized streamwise velocity/elevation correlation profiles at various downstream locations
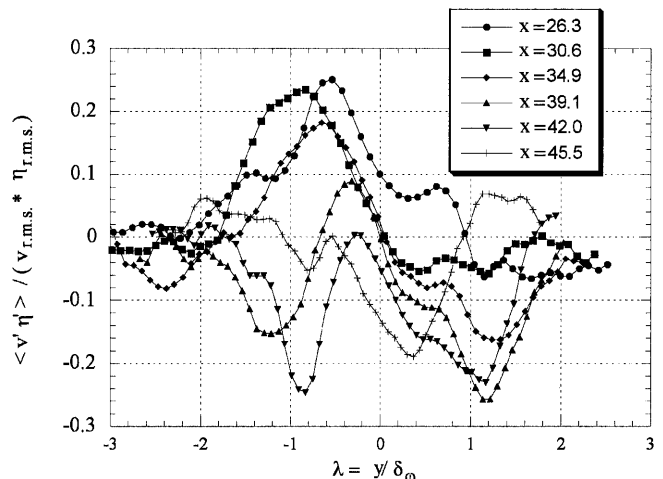

Fig. 16. Mean spanwise velocity/elevation correlation coefficient profiles at various downstream locations
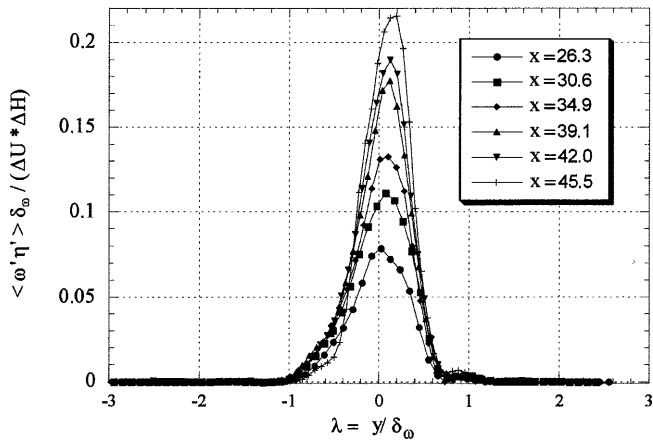
388

Fig. 17. Mean normalized vertical-vorticity/elevation correlation profiles at various downstream locations
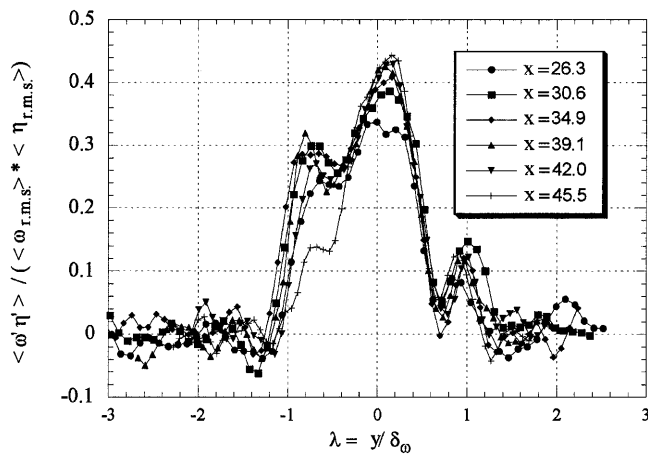

Fig. 18. Mean vertical-vorticity/elevation correlation coefficient profiles at various downstream locations

towards the high-speed side. Furthermore, Fig.18 shows that within this range, these correlations are strong, as the correlation coefficients reach a maximum value of ~ 0.4. While it is not known why the correlation peaks are shifted to the high speed side, it is clearly evident from these results that the free-surface deformations best correlate with the near-surface normal-vorticity-component field. In fact, this confirms the work of Dommermuth et al. (1994), who showed that for low Froude numbers, the surface elevation is hydrostatically balanced by the vortically-induced pressure, indicating it is the vorticity that is directly responsible for the free surface deformations.

389

George et al. (1984) showed that the spectra of a homogeneous constant-mean shear flow contains three terms, a dominant 2nd moment turbulence–mean shear interaction term with a $-11/3$ slope, a 3rd moment turbulence–mean shear interaction with a -3 slope, and a turbulence–turbulence interaction with a $-7/3$ slope. As pressure and free-surface deformation are directly related, this provided us with a unique opportunity to calculate the near-surface pressure spectra, and confirm these findings. Figure 19 shows the pressure spectra at various spanwise locations across the shear layer at 35 cm downstream from the edge of the splitter plate. For $x/\delta_\omega \leq |1.5|$, the spectra shows a logarithmic distribution with a $-10/3$ slope. It should be noted that this slope represents the contributions of all three terms described by George et al., since our measurements could not separate their effects. However, as the measured slope of $-10/3$ is very close to the theoretically derived value of $-11/3$, the dominance of the 2nd moment turbulence–mean shear interaction can be inferred for this flow.

7
Conclusion and results
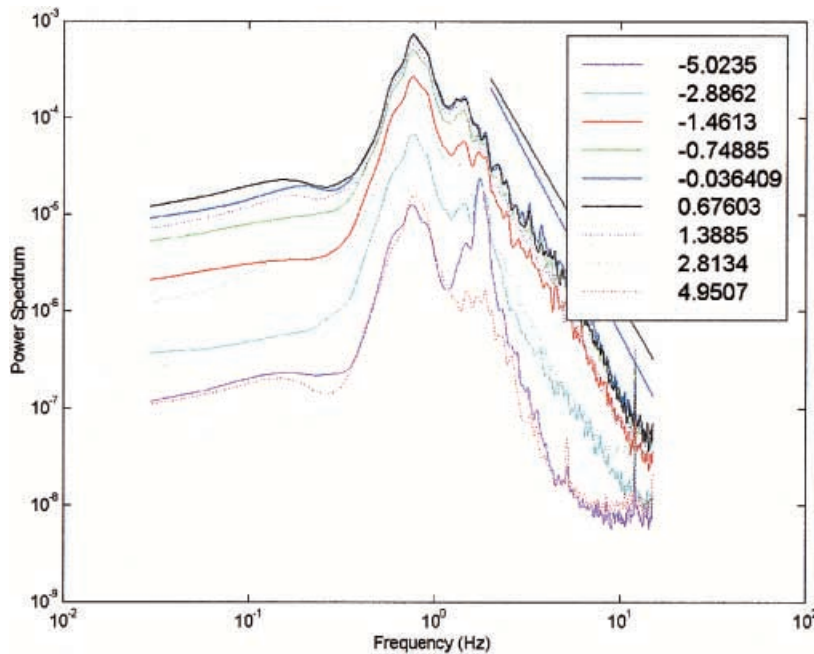A new approach for simultaneous free-surface deformation and near-surface kinematic measurements is

Fig. 19. Spanwise pressure spectra for various $y/\delta\omega$ at $x = 35$ cm

presented, which integrates DPIV and the more recently developed reflective FSGD method. This technique is applied to study the interaction of a vertical shear layer with a free-surface and in particular, the correlation between the free-surface deformation and the velocity and vorticity fields. As this technique provides a global two-dimensional view of the deformation and kinematic fields, this approach provides an invaluable tool for understanding of the physics of the free-surface flows. Preliminary results show that the near-surface deformation best correlates with the near-surface normal-component-vorticity field, as was predicted by Dommermuth et al. Calculation of the near-surface pressure spectra shows an inertial slope of $-10/3$, indicating that the interaction of the 2nd moment turbulence with the mean shear is dominant for the present shear layer.

In the future, we plan to find new ways to further reduce the uncertainty levels. We also plan to combine the FSGD method with stereo DPIV in order to allow for acquisition of all components of velocity, as well as deformation. This will then allow us understand the role of the turbulent kinetic energy, as well as the pressure-velocity term, in near surface flows.

References

Balschbach G; Klinke G; Jähne B (1998) Multichannel shape from shading techniques for moving specular surfaces. In: Burkhardt H; Neumann B (eds) Computer vision, Proceedings of EDCV '98, vol II, Lecture Notes in Computer Science 1407. Springer, Berlin Heidelberg New York, pp 170–184

Cox CS (1958) Measurement of slopes of high-frequency wind waves. J Mar Res 16: 199

Dabiri D (2000) Interaction of a vertical shear layer with a free surface. Submitted to J Fluid Mech

Dabiri D; Westerweel J; Jeon D; Shan J (1995) On the effects of window shifting and image windowing for improved accuracy of velocity measurements for DPIV. American Physical Society, 48th-Annual Meeting of the Division of Fluid Dynamics, 19–21 November, Irvine, Calif

Dabiri D; Zhang X; Gharib M (1997) Quantitative visualization of three-dimensional free surface slopes and elevations. In:

Nakayama Y (ed) Atlas of visualization. CRC Press LLC Boca Raton

Dommermuth DG; Novikov E; Mui R (1994) The interaction of surface waves with turbulence. free-surface turbulence ASME Meeting, FED-vol 181, pp 123–140

Gharib M; Dabiri D (2000) Digital particle image velocimetry. In: Smits AJ; Lim TT (eds) Flow visualization: techniques and examples. Imperial College Press, London, pp 123–148

George WK; Beuther PD; Arndt REA (1984) Pressure spectra in turbulent free shear flows. J Fluid Mech 148: 155–191

Hering F; Balschbach G; Jähne B (1996) A novel system for the combined measurement of wave- and flow-fields beneath wind induced water waves. In: Kraus K; Waldhausl P (eds), Proceeding of 18th International Congress for Photogrammetry and remote sensing Int Arch Phot Remote Sensing vol 31, Part B5: 231–236

Jähne B (1997) Image processing for scientific applications. CRC Press, New York

Klette R; Schluns K; Koschan A (1998) Computer vision – spatial data from images. Springer, Singapore Berlin Heidelberg

Westerweel J; Dabiri D; Gharib M (1997) The effect of a discrete window offset on the accuracy of cross-correlation analysis of digital PIV recordings. Exp Fluids 23: 20–28

Wierzimok D; Hering F; Melville WK; Jähne B (1996) Combined wave and flow field visualization for investigation of short-wave/long-wave interaction. In: Donelan MA; Hui WH; Plant WJ (eds) Proceedings, The air–sea interface, radio and acoustic sensing, turbulence and wave dynamics, Marseille, 24–30 June 1993, University of Miami, Miami, Flo, pp. 133–138

Willert C; Gharib M (1991) Digital particle image velocimetry. Exp Fluids 10: 181–193

Zhang X (1995) Capillary-gravity and capillary waves generated in a wind wave tank: observations and theories. J Fluid Mech 289: 51–82

Zhang X (1996) An algorithm for calculating water surface elevations from surface gradient image data. Exp Fluids 21: 43–48

Zhang X; Cox CS (1994) Measuring the two-dimensional structure of a wavy water surface optically: a surface gradient detector. Exp Fluids 17: 225–237

Zhang X; Dabiri D; Gharib M (1996) Optical mapping of fluid density interfaces: concepts and implementations. Rev Sci Instrum 67(5): 1858–1868